Check for updates

Synthesis of MnCoO/CNT nanoflakes for the photocatalytic degradation of methyl orange dye and the evaluation of their activity against *Culex pipiens* larvae in the purification of fresh water†

Rania A. Mohamed, [ID] *[ab] Niveen M. Ghazali,[c] L. M. Kassem,[d] Elsayed Elgazzar[e] and Wageha A. Mostafa[f]

Researchers worldwide have been looking forward to using novel ways to purify fresh water containing pollutants and disease vectors. In the current work, nanoparticles were introduced as a promising technique for cleaning water and saving human health and living organisms. The nanocomposites, MnCoO and MnCoO/CNTs, were fabricated by a cost-effective co-precipitation method. Phase and molecular structures were investigated by XRD and Raman spectroscopy. The samples exhibited polycrystalline nature of binary phase and weak crystallinity. The elemental composition was recorded by EDX spectra, revealing the purity of the nanoparticles. The surface morphology and particle distribution were described using SEM and TEM micrographs, indicating that MnCoO/CNTs are nanoflakes with a large surface area. The optical parameters include α, E_g, n, k, which were identified from $T\%$ and $R\%$ measurements, suggesting that MnCoO has a direct band gap that reduced with the CNT support. The photocatalytic activity of MnCoO/CNTs was examined for the degradation of methyl orange dye with an efficiency of $\sim$90.97% over 0.6 g L^{-1} within 50 min under UV irradiation. In the larvicidal activity, the micrograph images revealed the impact of the nanoflake particles on the 4th instar larvae, where the enzymatic activity of esterases acetylcholinesterase, α- and β-carboxylesterase, and transaminases drastically decreased with the MnCoO/CNT ratio.

1 Introduction

Because of industrial revolution, the release of chemical wastes such as organic dyes into water poses a great threat to environment and human health. In addition, these dyes are considered a convenient habitat for different species of mosquitoes that act as vectors of pathogens and parasites. Moreover, these dyes have the ability to attract female

[a]Department of Biology, Deanship of Educational Services, Qassim University, P. O. Box: 5888, Unaizah 56219, Qassim, Saudi Arabia. E-mail: R.mohamed@qu.edu.sa

[b]Parasitology Department, Faculty of Veterinary Medicine, Zagazig University, P. O. Box 44519, Zagazig 44516, Egypt. E-mail: raniaatef@zu.edu.eg

[c]Department of Pharmaceutical Chemistry and Pharmacognozy, Unaizah College of Pharmacy, Qassim University, P. O. Box: 5888, Unaizah 51911, Qassim, Saudi Arabia. E-mail: N.ghazali@qu.edu.sa

[d]Department of Pharmacy Practice, Unaizah College of Pharmacy, Qassim University, P. O. Box: 5888, Unaizah 51911, Qassim, Saudi Arabia. E-mail: L.Mahmaud@qu.edu.sa

[e]Department of Physics, Faculty of Science, Suez Canal University, Ismailia, Egypt. E-mail: Elsayed_Mohsen@science.suez.edu.eg

[f]Entomology Section, Zoology Department, Faculty of Science, Zagazig University, Zagazig 44519, Egypt. E-mail: WAMustafa@science.zu.edu.eg

† Electronic supplementary information (ESI) available. See DOI: https://doi.org/10.1039/d2ra04823j

mosquitoes to live, feed, and lay their eggs, causing the aquatic environment an endemic area for diseases. For instance, *Culex pipiens* is the main vector of lymphatic filariasis and yellow fever, causing infection for millions of people worldwide.[1,2] Accordingly, the degradation of dyes using novel and creative strategies has received great attention from the scientific community. Various catalysts including metals, metal oxides, and hybrid nanocomposites were developed for this purpose. For example, silver (Ag), zinc telluride (ZnTe), palladium-doped zinc oxide (ZnO), and manganese oxide (MnO_2) nanostructures have been successfully applied as photocatalysts. Among the aforementioned nanomaterials, manganese oxide nanoparticles with high chemical stability, a large surface-to-volume area, and a variety of oxidation states display attractive features in various nanotechnology fields extending from materials science, chemical engineering to biotechnology. Further, cobalt oxide has been investigated as an influential catalyst based on its high chemical reactivity. Cobalt oxide has different oxidations, CoO, Co_2O_3, CoO_2, and Co_3O_4, in which Co_3O_4 and CoO are the most stable forms with excellent thermal and chemical stabilities. Several studies in the literature have reported the incorporation of manganese oxide with noble metals for the degradation of textile dyes.[3,4] Siddique *et al.*, have fabricated

zinc manganese oxide *via* a mechanochemical approach for the improvement of photocatalytic activity.[4]

Moreover, CNTs of exceptional physicochemical characteristics have been used in a wide range of applications. Doping metal oxides with appropriate amounts of CNTs will produce nanocomposites with desired aspects. In fact, CNTs have drawn attention owing to their unique electrical and mechanical aspects and seamless cylinder structure. In addition, CNTs have a large numbers of adsorption sites, which would be useful for adsorbing active sites of dye and toxic molecules. Here, the nanocomposite MnCoO/CNTs displayed great photocatalytic activity because CNTs are good electron acceptors that play an important role in rising free charge carriers.[5,6] It is worthy to mention that mosquitoes are completely holometabolic with most of the life cycle happening in fresh water. Therefore, the control of the larval stages using nanoparticles plays an important role in reducing the negative effect on human and animal health. Recently, some studies in the literature have reported the destructive action of hybrid nanomaterials toward harmful organisms such as bacteria and *C. pipiens* mosquito larvae with biocidal activities.[7,8] In addition, ingestion or inhalation of these nanocomposites may alter the insect's biochemical activity, leading to an understanding of the nanocomposite mechanism. Thus, many enzymes including, esterases, phosphatases, and transaminases were evaluated to confirm the effect of nanoparticles (NPs) on the enzyme performance related to insect resistance. This effect leads to a disruption of various physiological processes in the tested larvae. Insects' esterase enzymes are responsible for many vital physiological processes involving digestion, molting, reproduction, and metabolism of hormones. In the nervous system, acetylcholinesterase has a very high stimulation action, as it is responsible for terminating nerve impulses by stimulating the hydrolysis of the neurotransmitter acetylcholine.[9] Carboxylesterases can degrade a diversity of carboxylic acid esters as well as play a role in the detoxification of pesticides to less poisonous compounds. Additionally, phosphatases control the phosphorylation of proteins present in cells, metabolism of carbohydrates and nucleotides, and transfer of energy by ATP. Thus, esterases and phosphatases of various physiological importance are used as precise and sensible biomarkers to assess the toxicity of the insecticides on pests and vectors. Further, glutamic oxaloacetic transaminase (GOT) and glutamic pyruvic transaminase (GPT) are the main enzymes in the formation of gluconeogenesis, non-essential amino acids, nitrogen compound metabolism, and related to the metabolism of protein.[10] Techniques such as hydrothermal processes, sol–gel methods, microwave irradiation, chemical vapor deposition, and solid-state thermal decomposition have been used for manufacturing nanostructured materials.[1,6] In the current study, a simple, available, and low-cost chemical technique was utilized to fabricate the nanocomposites MnCoO and MnCoO/CNTs. XRD, Raman spectroscopy, EDX, SEM, TEM techniques and optical absorbance spectra were investigated to characterize the prepared nanomaterials. The findings revealed that MnCoO/CNT nanoflakes are promising composites with distinguished and magnificent photocatalytic performance that can be effectively applied for the photodegradation of organic methyl orange (MO) dye and the larvicidal activity in water treatment.

2 Experimental section

2.1. Chemicals

Manganese chloride tetrahydrate ($MnCl_2 \cdot 4H_2O$), cobalt chloride dehydrate ($CoCl_2 \cdot 2H_2O$), sodium hydroxide (NaOH), carbon nanotubes (CNTs), methyl orange (MO dyes), cacodylate buffer, glutaraldehyde, osmium tetroxide (OsO_4), ethanol, and acetone were used. All reagents were obtained from Merck and Alfa Aesar Company.

2.2. Synthesis of the nanocomposites

Manganese cobalt oxide (MnCoO) Mn : Co 60 : 40 wt% was prepared by dissolving 2.70 g manganese chloride tetrahydrate ($MnCl_2 \cdot 4H_2O$) into 30 mL double-distilled water using a magnetic stirrer. Then, 1.80 g cobalt chloride dehydrate ($CoCl_2 \cdot 2H_2O$) was separately dissolved into 40 mL double-distilled water. After that, $CoCl_2$ was added to $MnCl_2$ with continuous stirring for 3 h. A sodium hydroxide (NaOH; 50 mL) solution was added dropwise into the mixture until a homogenous precipitate was formed at pH ∼ 9. The resulting precipitate powder was filtered and washed several times with distilled water. Then, it was dried at 80 °C and eventually annealed at 400 °C for 3 h. In order to prepare the nanocomposite MnCoO/CNTs, 10 mL of CNT solution (0.2 g L^{-1}) was added to 25 mL MnCoO (1 g L^{-1}) with continuous stirring for 5 h. Thereafter, the mixture was subjected to heat treatment using a microwave oven for half an hour. The obtained precipitate powder was centrifuged and eventually dried at 80 °C for 10 h.

2.3. Characterization

The phase and structure of MnCoO and MnCoO/CNTs were characterized using an X-ray diffractometer (XRD; JEOL, JDX-7E) operating at 2θ angle ranging from 10° to 65°. Raman spectroscopy (Horiba Lab RAM HR Evolution) was performed to define the molecular interaction and phase content. The surface morphology and elemental composition were examined using scanning electron microscopy (SEM, JEOL JXA-840A) with energy dispersive X-ray analysis (EDX). The microstructure and mean size of pure and composite MnCoO were visualized by TEM (TEM; Hitachi-H-7500, Japan). A spin coater (SpinNXG-P1AC) was used to fabricate the nanocomposite thin films. A 500 W Xe lamp (UXL-500D) was utilized for photocatalysis investigation. A UV-vis spectrophotometer JASCO (V-570) was utilized to evaluate the optical properties of the thin films and the photocatalytic performance.

2.4. Evaluation of the photocatalytic activity

The photocatalytic activity of MnCoO/CNT nanostructures were studied *via* screening the photodegradation of methyl orange (MO) dye in an aqueous solution under UV light irradiation. First, 30 mg of methyl orange (MO) was dissolved in 1000 mL of

water. Then, MnCoO/CNTs of different concentrations (0.3 g L^{-1}, 0.6 g L^{-1}, and 0.9 g L^{-1}) were added to the prepared solution of methyl orange dye. The photocatalytic degradation of MO was carried out at room temperature of ~27 °C, a MO dye concentration of 30 mg L^{-1}, and MnCoO/CNT catalyst concentrations of 0.3 g L^{-1}, 0.6 g L^{-1}, and 0.9 g L^{-1}. The MO photodegradation efficiency (%) was determined using a UV-vis spectrophotometer. The reusability test of the MnCoO/CNT catalyst was investigated. Despite the possibility to partially separate the MnCoO/CNT catalyst from the mixture after the reaction *via* centrifugation (2000 round per minute), a catalyst cannot return to its original state because of the very tiny amount obtained under the influence of centrifugation and washing several times. Therefore, it is difficult to keep the efficiency of the catalyst with more cycles of reuse.[11]

2.5. Mosquito rearing

C. pipiens larvae were brought from Medical Entomology Institution, Cairo, Egypt. They were reared at a temperature of 27 °C ± 2 °C with a relative humidity (R.H.) of 80 ± 5% and a photoperiod of 14 h light: 10 h darkness. *C. pipiens* adults were bred in cages (30 × 30 × 30 cm) and fed with 10% sugar solution. In addition, the females set eggs three days after sucking blood. Eggs were hatched, immature stages were raised in plastic dishes of dimension 25 × 25 × 5 cm and grown up on fish food.

2.6. Biochemical analysis

Biochemical analysis was carried out to investigate the enzyme responses of the treated 4th larval instars with MnCoO and MnCoO/CNTs at a mortal concentration of 50 mg L^{-1} for 24 h and compared with the control.

2.6.1. Preparation of whole-body homogenates. The larval body surface was rinsed with deionized water and dried with a tissue paper for the final assessment of total protein and enzymatic activity. The cleaned larvae were collected in Eppendorf tubes (kept in ice) using a Teflon hand homogenizer in 1 mL 0.9% saline. The total body homogenates were centrifuged at 10 000 rpm at 4 °C for 10 min and the pure supernatants were preserved at 4 °C for many tests such as the estimation of protein concentration: the colorimetric estimation method was used according to a previous study[12] with little modification. This method depends on the protein in the existence of alkaline cupric sulfate. The protein showed a violet purple color and the absorbance of the specimens against a blank Biuret reagent was determined at 546 nm wavelength.

2.6.2. Enzymatic activity. Acetylcholinesterase activity in the whole homogenate larval body was spectrophotometrically determined according to the procedure reported in the literature.[13] In addition, acid and alkaline phosphatase activities were measured by the procedures recorded in a previous study.[14] Moreover, activities of α-carboxylesterases and β-carboxylesterases were measured calorimetrically by applying substrates α-naphthyl acetate and β-naphthyl acetate, respectively,[15] which produced a strong blue-purple color referring to α-naphthol or a strong red-purple color indicating β-naphthol, in which colors were measured spectrophotometrically at 600 and 555 nm for α-naphthol and β-naphthol, respectively. Further, GOT and GPT activities were detected by a previously reported method[16] using the Bioadwic kit, where the enzymatic activity was determined calorimetrically using a spectrophotometer at 546 nm.

2.7. Scanning electron microscopy (SEM)

The infected larvae were fixed in 2.5% glutaraldehyde (Sigma) for 2 h and washed with 0.1 M cacodylate buffer (pH 7.2) for approximately 15 min. Then, osmium tetroxide (OsO_4) was added for post-fixation for 2 h. The samples were cleaned with a buffer, dehydrated in a series of diluted ethanol, embedded in an acetone solution and, eventually, coated with iridium vapor using an imaging sputter coater (Model, EMS 150T ES). The specimens were investigated by SEM (Helios Nano-Lab. 400) at 10 kV.
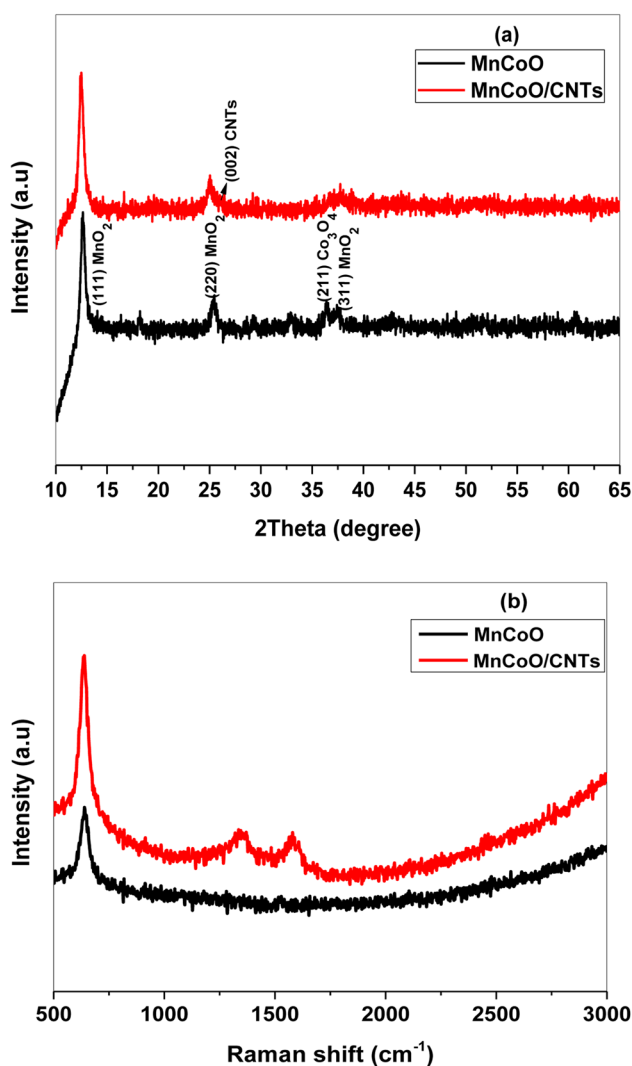

Fig. 1 (a) XRD patterns and (b) Raman spectra of MnCoO and MnCoO/CNT nanocomposites annealed at 400 °C.
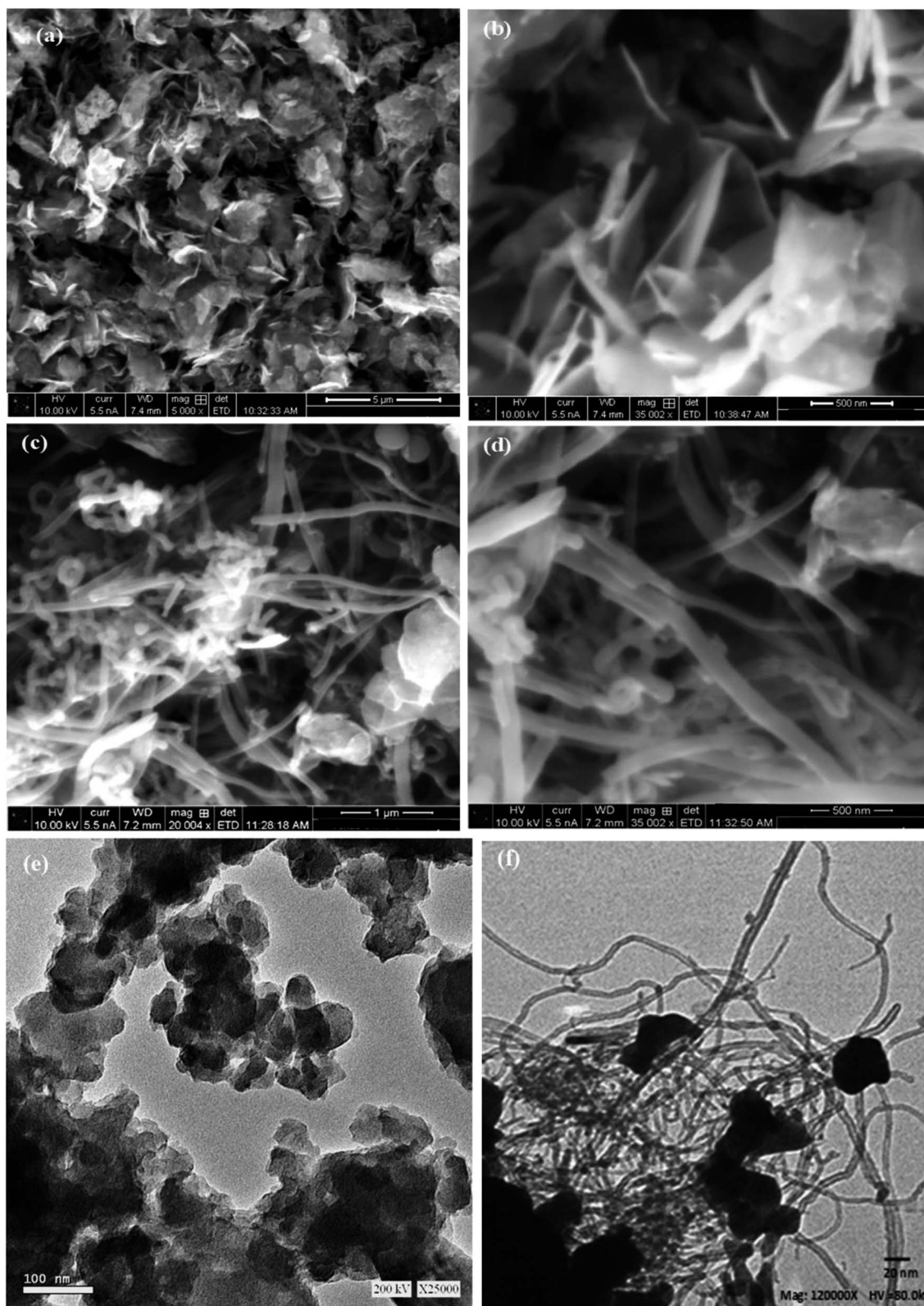
Fig. 2 SEM images of (a and b) MnCoO and (c and d) MnCoO/CNTs at different magnifications and the TEM images of (e) MnCoO and (f) MnCoO/CNTs.

2.8. Statistical analysis

In biochemical analysis, every test was examined with three replicates, and the significance degree of control and treated larvae was counted using one-way analysis of variance (ANOVA) SPSS version 14.

3 Results and discussion

3.1. Microstructure analysis

The crystallographic structure of MnCoO and MnCoO/CNTs was identified using the X-ray diffraction pattern recorded at room temperature. Fig. 1a shows the nanostructure of the characteristic diffraction peaks at 12.48°, 25.35°, 36.30°, and 37.64°, corresponding to the (110), (200), (211), and (311) planes, respectively. The spectrum exhibited a binary phase composed of manganese oxide (MnO_2) and cobalt oxide (Co_3O_4). The phase segregation is owing to the high loading concentration of cobalt ions within the host manganese oxide lattice. Many factors such as dopant concentration, any difference in electronegativity and dissimilar ionic radii between the host molecules and dopant atoms can have

impacts on the microstructure leading to phase segregation. Most of the peaks observed in the pattern are very weak, suggesting poor crystallinity that may be associated with a low annealing temperature. The wider characteristic reflection peak observed at $2\theta = 26.05°$ in the spectrum was ascribed to CNTs that incorporated the MnCoO framework.[17–20] A slight shift to a lower 2θ angle in the main peaks of the (110) and (220) planes is attributed to the lattice disorder induced by doping ions.[20,21]

Fig. 1b demonstrates the Raman spectra carried out at room temperature in the wave number range of 500 cm^{-1} to 3000 cm^{-1}. The band observed at the wave number 641 cm^{-1} was attributed to the Mn–O–Co stretching frequency. MnCoO/CNTs show a strong intense peak at ~638 cm^{-1} with a slight peak shift toward a lower wave number, which may result from the lattice strain and create new energy levels into the energy gap. The Raman modes located at 1345 cm^{-1} and 1577 cm^{-1} were indexed to the CNT molecules.[21–23] The chemical composition and purity of the prepared samples were checked out using EDX spectra. As described in Fig. S1a,† manganese cobalt oxide
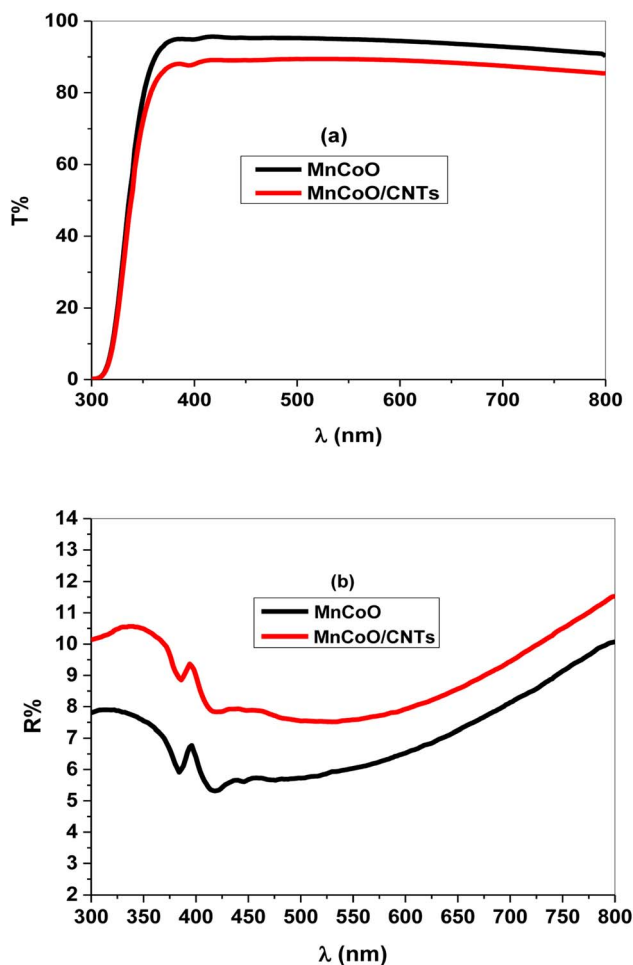

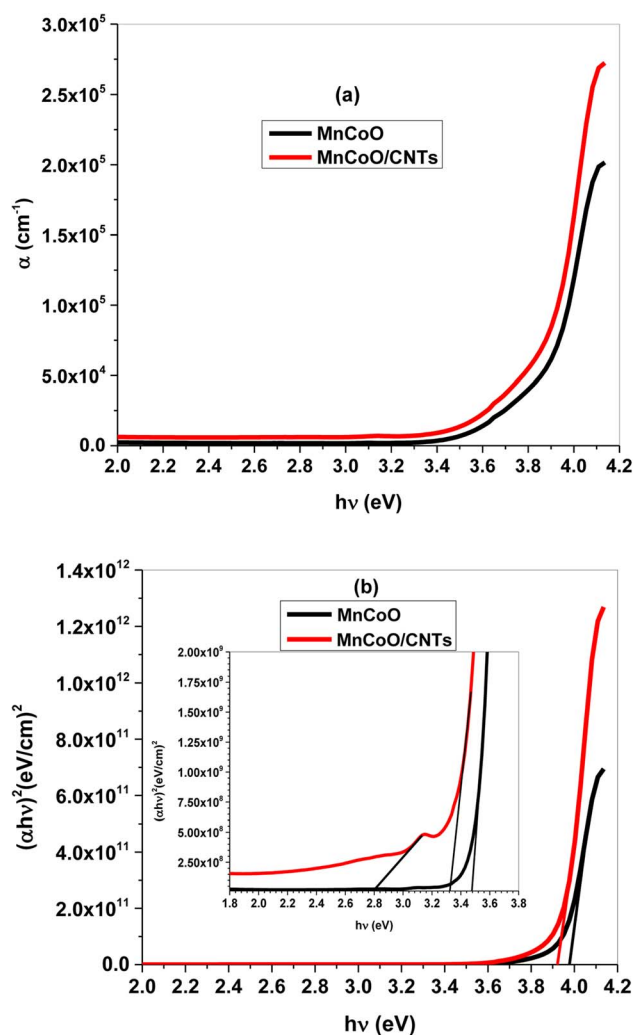**Fig. 3** (a) Transmittance (*T*%) and (b) reflectance (*R*%) spectra of the nanocomposite thin films.

Fig. 4 (a) Absorption coefficient (α) as a function of photon energy ($h\nu$) and (b) energy gap (E_g) plot of the fabricated thin films.

consists of the elements Mn, Co, and O. The carbon peak observed in the spectrum (Fig. S1b†) at 0.277 keV clearly revealed the integration of MnCoO with CNTs.[21,23]

The SEM micrograph was examined at different magnifications to describe the surface morphology of the nanocomposites. As can be seen in Fig. 2a and b, the particles of MnCoO are uniformly distributed in nanoflake shapes with high density. Besides, the morphological characteristics revealed that MnCoO/CNTs have a large surface area (Fig. 2c and d). Fig. 2d shows the reduction in the nanoflakes due to the CNT substitutions.[21,24,25] The TEM images of MnCoO and MnCoO/CNTs are shown in Fig. 2e and f. As observed from the images, MnCoO is composed of high-density ultrathin nanoflakes, which are irregularly distributed on the surface (Fig. 2e). The mean size of the particles was determined to be approximately 160 nm. Fig. 2f shows the nanocomposite MnCoO/CNTs with a large surface area, in which some of the nanoflakes were aggregated together due to the size confinement effect.[26,27]
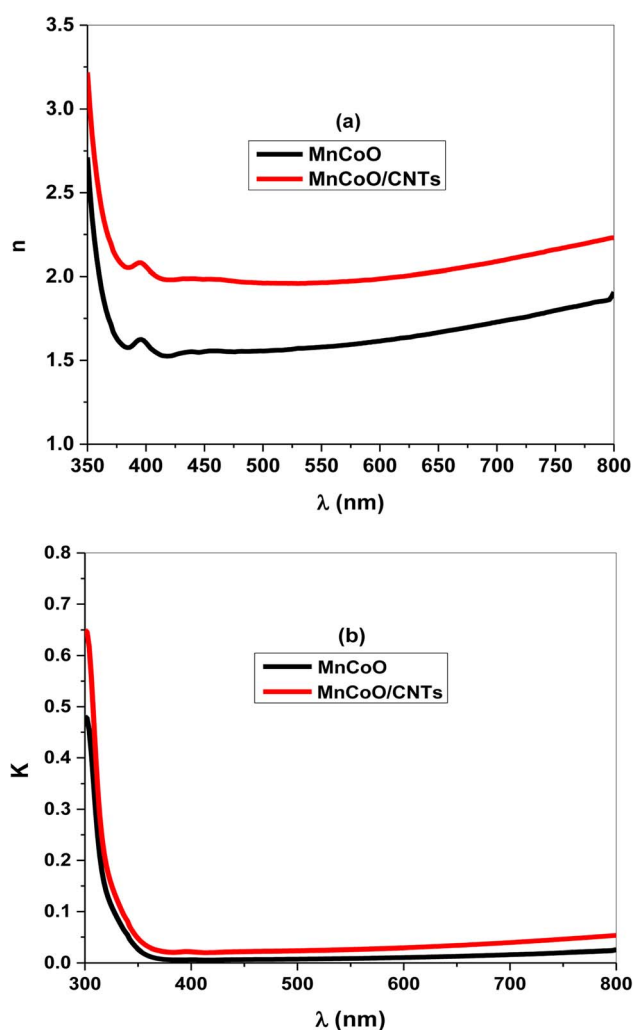
3.2. Optical characterization

Fig. 3a and b illustrate the optical transmittance ($T\%$) and reflectance ($R\%$) spectra of MnCoO and MnCoO/CNT thin films coated on glass substrates through the UV-vis region. The films exhibited high optical transmittance of sharp absorption edge at ~335 nm attributed to the interband electron transitions (Fig. 3a). Further, the transmittance profile of MnCoO/CNTs displayed values less than 90% in the visible region. Fig. 3b describes the reflectance spectra of valleys and peaks associated with light scattering and optical-electron interaction.[28,29] It is worthy to note that the reflectance peak is related to photon interference, while the valleys are associated with the lattice disturbance and increase in strain. The absorption coefficient (α) was expressed using the following formula:[30]

$$\alpha = \frac{1}{d} \ln \left[\frac{(1 - R^2)}{2T} + \sqrt{\frac{(1 - R)}{4T^2} + R^2} \right] \quad (1)$$

Fig. 4a shows the absorption band of MnCoO nanostructures at 4.10 eV inside the UV spectrum shifted to a lower energy with the CNT support. This is owing to the strong light absorption and increase of free charge carriers, causing more electrons to jump to the conduction band. The energy gap (E_g) was evaluated from $(\alpha h\nu)^2$ against ($h\nu$) graph according to the following Tauc relation:[30]

$$\alpha = \frac{A}{h\nu} \left(h\nu - E_g \right)^n \quad (2)$$

where A is an independent constant and $n = 1/2$ for direct band gap transition. The values of E_g were calculated to be 3.98 and 3.92 eV for MnCoO and MnCoO/CNTs, respectively. Another allowed optical transitions were detected at 3.47 and 3.32 eV
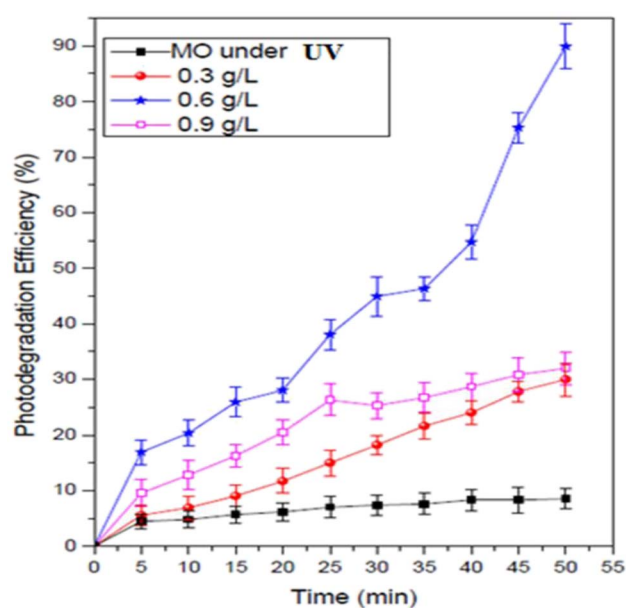

Fig. 5 (a) Refractive index (n) and (b) extinction coefficient (k) of the nanocomposite-coated thin film.

Fig. 6 Photodegradation efficiency (%) of the MO dye (30 mg L^{-1}) and MO with the MnCoO/CNT catalyst under UV irradiation.

associated with the strong optical-electron interaction. The energy gap reduction was related to the presence of CNTs, resulting in more additional energy levels inside the optical band gap of the host material MnCoO. Further, an optical transition was observed at 2.81 eV owing to the structure disorder of the nanocomposite MnCoO/CNTs and the formation of localized energy levels close to the conduction band (Fig. 4b).[31,32]

It is well known that the refractive index (n) and extinction coefficient (k) are important optical parameters for studying the optical and dielectric properties of the synthesized thin films are described by the following relations:[30,33]

$$n = \left(\frac{1+R}{1-R}\right) \pm \sqrt{\frac{4R}{(1-R)^2} - K^2} \quad (3)$$

$$K = \frac{\alpha\lambda}{4\pi} \quad (4)$$

Fig. 5a and b illustrate n and k of the nanocomposites as a function of the wavelength. As shown in Fig. 5a, the refractive index of a UV peak in the interband transition region increased with CNT replacements and strong light absorption.[29] Further, MnCoO/CNTs exhibited a normal refractive index in the visible region with values greater than 2. Fig. 5b displays the extinction coefficient of low values in the visible region, which sharply increased in the UV spectrum due to the optical absorption.[32,33]

3.3. Photocatalytic activity

The scheme in the current study depends on the investigation of the possible reactions (methyl orange adsorption on the surface of MnCoO/CNTs and direct photodegradation of methyl orange without MnCoO/CNTs catalyst). Therefore, a series of experiments were executed to calculate the photocatalytic performance of MnCoO/CNTs to approve that the drop in MO dye concentration is entirely thanks to the photocatalytic activity. The blank experiments were carried out: (i) the
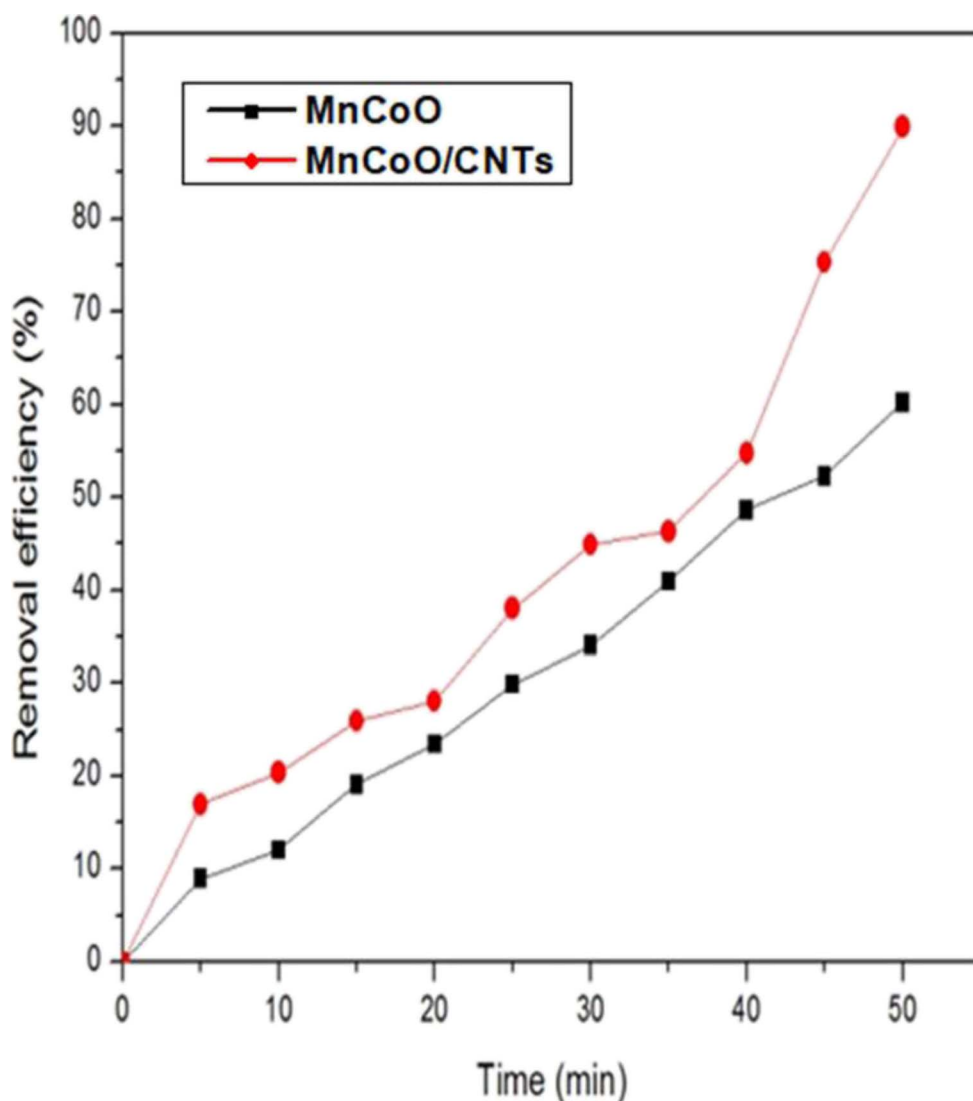

Fig. 7 Removal efficiency (%) of the MO dye (30 mg L^{-1}) with 0.6 g L^{-1} of the fabricated catalysts under UV irradiation.

adsorption of the methyl orange dye on the surface of MnCoO/CNT nanocomposites was achieved in dark environments. The adsorption–desorption of MO dye affected by MnCoO/CNT concentrations and other variable such as pH was investigated.[34,35] (ii) The experiment of methyl orange degradation was done under the direct illumination of the methyl orange solution by UV light without the MnCoO/CNT catalyst.

It can be seen that without the catalyst, only a minor amount of the methyl orange concentration was reduced. Fig. 6 shows the impact of MnCoO/CNTs on the photodegradation behavior of methyl orange dye. It can be seen that, at 0.6 g L^{-1} catalyst concentration, the photodegradation efficiency of the methyl orange exhibited the highest value and it was found to be 90.97% within 50 minutes. It is very clear to show that the photocatalytic activity was improved by inserting MnCoO/CNT catalysts. Moreover, the photodegradation efficiency of MnCoO nanoparticles was performed to compare it with the efficiency of MnCoO/CNTs, as depicted in Fig. 7. As seen, the efficiency of 0.6 g L^{-1} MnCoO used to degrade the MO dye was 60% at 50 min, whereas, at the same concentration, MnCoO/CNTs were able to degrade 90.97% of the MO dye. The results indicated the significant impact of CNT addition on the degradation mechanism owing to the easy electron transfer between manganese cobalt oxide and CNTs as well as the increase in the surface area and free charge carriers without recombination. This result is strongly consistent with the structure and morphological study that clearly confirm the unique properties of CNTs. Furthermore, the UV-vis absorbance of MO dye and MO with different concentrations of MnCoO/CNT catalysts (0.3 g L^{-1}, 0.6 g L^{-1}, and 0.9 g L^{-1}) was examined under UV irradiation for 40 min. As shown in Fig. 8, the absorption band of MO dye detected at $\lambda \sim 470$ nm was decreased exhibiting a slight red-shift with the catalyst concentrations. As can be seen, the catalyst concentration of 0.6 g L^{-1} possessed the lowest absorption band, which can be explained by increasing the photoinduced charge carriers by the impact of the catalyst ratio under UV irradiation.[36,37]

3.4. MO photodegradation mechanism

The methyl orange adsorbed by MnCoO/CNTs surface, herein the nanocomposite serves as a light absorber and photocatalyst, when the energy ($h\nu$) of the UV is applied to the system. The electrons (e_{cb}^-) in the valence band are excited, under UV irradiation, to the conduction band.[38,39] Thus, an electron–hole pair was produced, due to electron transition in the valence band. The electrons induced from the UV energy react with molecular oxygen that was adsorbed on the surface of MnCoO/CNTs creating hydrogen peroxide (H_2O_2) and superoxide O_2^- radical anions:[39,40]
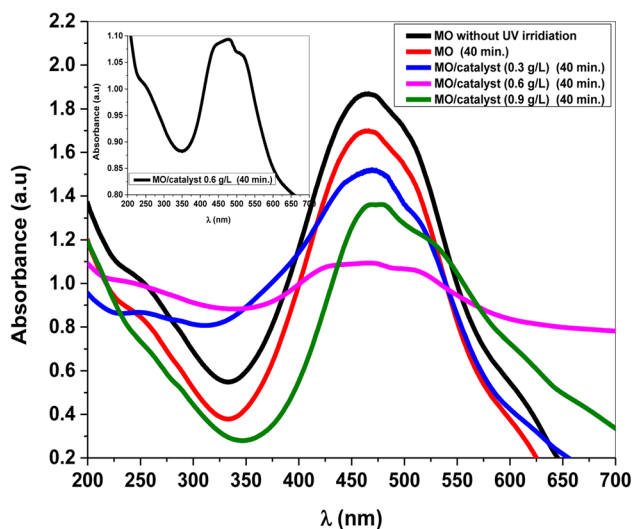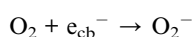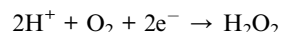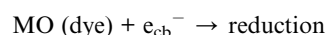
$$MnCoO/CNTs + h\nu \xrightarrow{UV} MnCoO/CNTs\left(e_{cb}^- + h_{vb}^+\right)$$
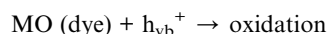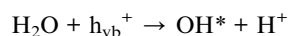
$$O_2 + e_{cb}^- \rightarrow O_2^-$$

Fig. 8 Absorbance peak of pure MO dye (30 mg L^{-1}) and MO with MnCoO/CNT catalysts under the impact of UV irradiation.
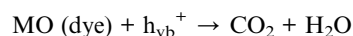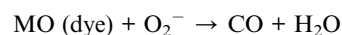
$$2H^+ + O_2 + 2e^- \rightarrow H_2O_2$$

Then, hydroxyl OH* radical was produced *via* the reaction of the hole (h_{vb}^+) generated from the UV irradiation and OH$^-$ or by H_2O oxidizing them to the hydroxyl radical:

$$H_2O + h_{vb}^+ \rightarrow OH* + H^+$$

$$H_2O_2 + O_2^- \rightarrow OH* + O_2 + OH^-$$

$$MO~(dye) + h_{vb}^+ \rightarrow oxidation$$

$$MO~(dye) + e_{cb}^- \rightarrow reduction$$

$$MO~(dye) + OH* \rightarrow degradation$$

In fact, the hydroxyl (OH*) radicals can degrade the methyl orange dye, as the (OH*) radical is a too strong oxidizing agent.

The holes (h_{vb}^+) and the (O_2^-) radical will contribute to the methyl orange degradation *via* the following reaction:

$$MO~(dye) + O_2^- \rightarrow CO + H_2O$$

$$MO~(dye) + h_{vb}^+ \rightarrow CO_2 + H_2O$$

From the viewpoint of the trading and industrial scale, the concentration of the catalyst is considered one of the most important parameters in photodegradation studies. Hence, it is very necessary to evaluate the optimum concentration of the catalyst that is required to degrade the methyl orange dye, to avoid the waste.

Fig. 9 demonstrates the impact of MnCoO/CNT catalyst concentrations on the degradation of the methyl orange dye. This experiment was carried out many times by changing the
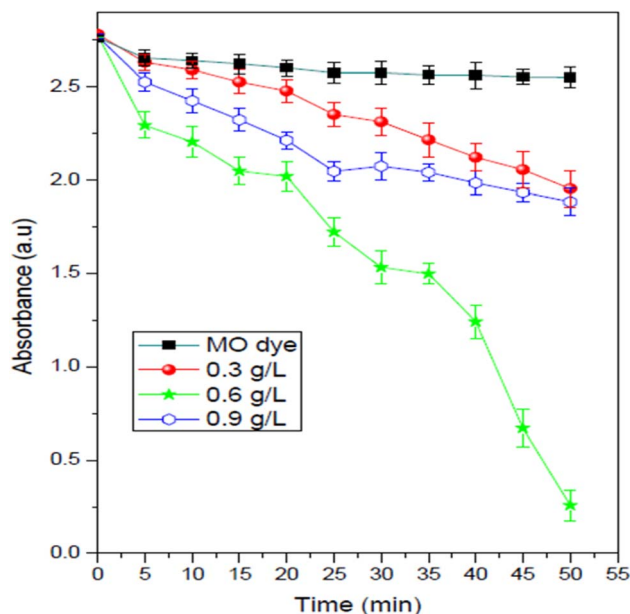
Fig. 9 Impact of the MnCoO/CNT catalyst ratio on the photo-degradation of MO dye (30 mg L^{-1}) under UV irradiation.

Table 1 Comparison of the degradation activities of various nano-material photocatalysts to the current MnCoO/CNT catalyst

Catalyst	Dyes	Efficiency (%)	Time	Ref.
MnCoO/CNTs	MO	90.97%	50 min	Current study
a-CNTs	MO	95%	90 min	37
CoMn$_2$O$_4$	Reactive black	95%	60 min	41
TiO$_2$–ZnO/RGO	MO	90%	40 min	41
ZnO@TiO$_2$ core–shell nanofibers	MO	90%	55 min	41
TiO$_2$ NPs	MO	99.8%	300 min	42
NiO nanosheets	Congo red	99%	100 min	41
Carbon doped SiO$_2$–TiO$_2$	RhB, MO	100%	52.5 min	41

nanoparticle percentage every time in the methyl orange solution from 0.3 to 0.9 g L^{-1}, keeping all the other parameters without changing. As shown in Fig. 9, the rate of MO degradation increased with the increase in MnCoO/CNT concentration, which may be attributed to the increase in active site number, and these active sites give high chances for receiving both light and guest molecules. In addition, at a higher concentration (0.9 g L^{-1}), the efficiency of MnCoO/CNTs catalytic decreased; this may be due to the decline in the amount of the active sites for light absorption at high MnCoO/CNT ratios, which may be attributed to the aggregation of the nanoparticles. The suspension turbidity is also a reason for the drop in MnCoO/CNT nanoparticle catalytic efficiency. The optimum concentration of MnCoO/CNTs to degrade the methyl orange dye was found to be 0.6 g L^{-1}. It is clear that, with the concentration 0.6 g L^{-1} of MnCoO/CNT catalyst, the brilliant activity of the methyl orange degradation was obtained, which was approximately 90.97% after 50 min of UV light irradiation. Moreover, the results obtained from the current study are compared with other results reported in the literature and summarized in Table 1. As observed, MnCoO/CNT catalysts achieved high efficiency for MO photodegradation. However, some of the catalysts achieved higher efficiency for MO and other dyes.[37,41,42] In fact, the photodegradation process depends on the pH value of the solution. The present study found that the photocatalytic efficiency (%) of MnCoO/CNT catalysts for the degradation of methyl orange dye is affected by the pH value. From this fact, the impact of pH in this experiment needs to be determined.[43]

Fig. 10 depicts the photocatalytic degradation of the methyl orange dye as a function of pH value. The pH values were selected as 3, 7, and 9 to cover the acidic, neutral and basic environment. As shown, at pH = 7, with 0.6 g L^{-1} of

nanocomposite concentration, high degradation of methyl orange dye was achieved, and with the increase in the pH value of the solution, the efficiency of the degradation process declines. It may be due to the repulsion force (the electrostatic nature) between MnCoO/CNTs and the dye methyl orange.[44,45] Besides, at a low pH value, the figure shows less degradation efficiency in an acidic medium owing to the dissolution of MnCoO/CNT nanoparticle catalyst.[44,46] Within fifty minutes, 90.97% degradation was achieved, beyond which, in comparison to other methods,[47] the photodegradation efficiency declined.[48]
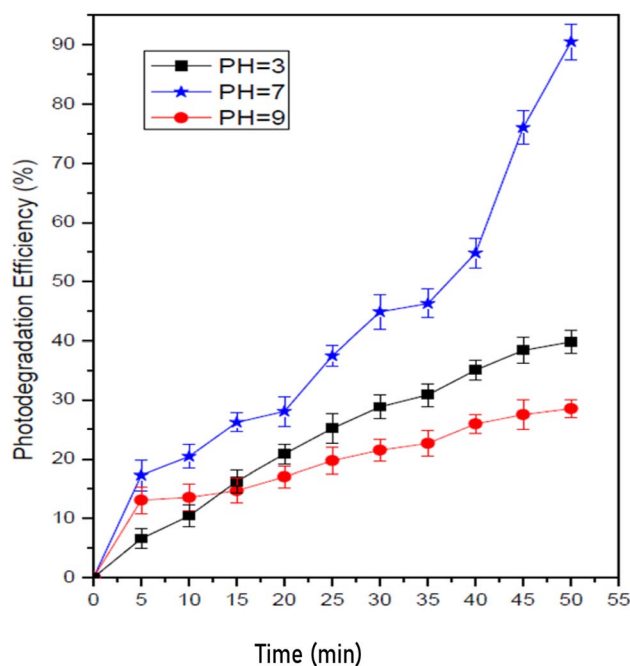

Fig. 10 Impact of pH on the photodegradation of the MO dye (30 mg L^{-1}) under UV irradiation.

Table 2 Enzymatic activity in whole-body homogenates of early 4th instar larvae of *C. pipiens* 24 h post-treatment with the nanocomposites MnCoO and MnCoO/CNTs[a]
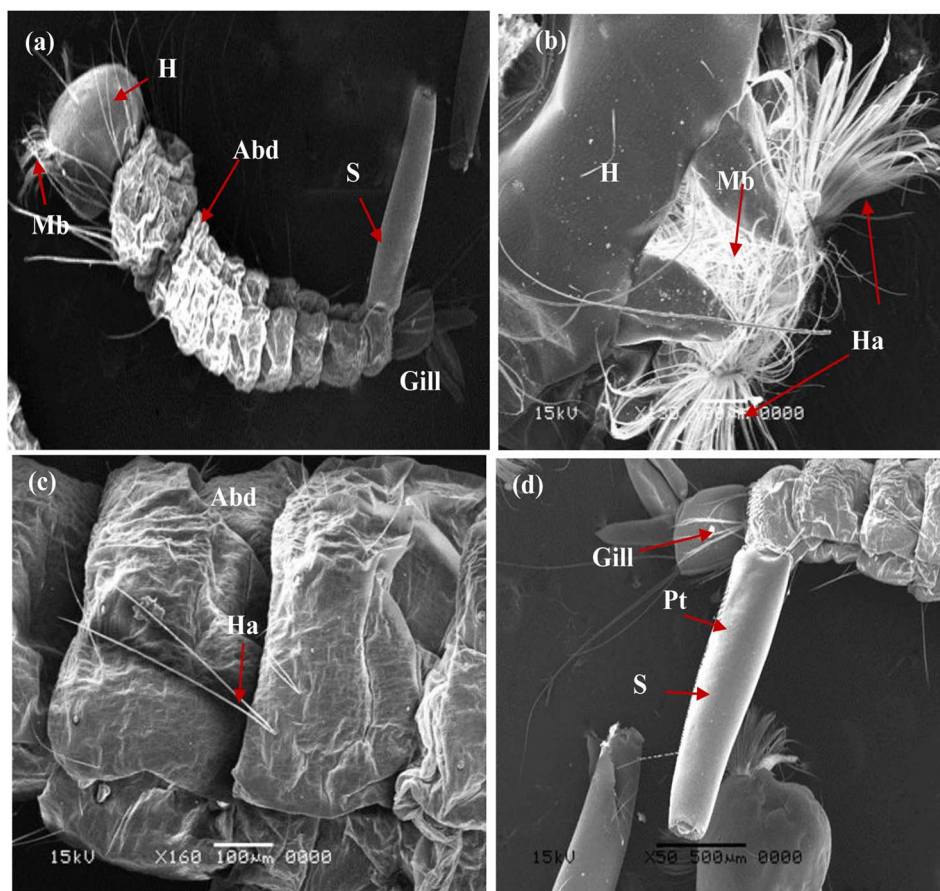
Enzymes	Control	MnCoO mean ± S.D	MnCoO/CNTs	Sig.
Total protein (mg g^{-1})	32.87 ± 5.89[a]	19.29 ± 3.24[ab]	5.87 ± 1.88[c]	0.01
Acid phosphatase (U g^{-1})	1041.61 ± 22.04[a]	504.72 ± 18.67[b]	555.36 ± 26.32[b]	0.01
Alkaline phosphatase (U g^{-1})	2113.37 ± 12.32[a]	74.86 ± 23.56[b]	200.25 ± 11.60[b]	0.001
Acetylcholinesterase (U g^{-1})	1858.92 ± 14.53[a]	815.57 ± 16.64[b]	264.49 ± 33.24[c]	0.01
α-Carboxylesterases (μg phenol per min per g)	5.681 ± 2.67[a]	1.816 ± 0.94[a]	0.2810 ± 0.01[b]	0.09
β-Carboxylesterases (μg phenol per min per g)	258.29 ± 14.70[a]	124.88 ± 6.32[a]	84.7001 ± 9.12[b]	0.02
GOT mg pyruvate per min per g	169.47 ± 1.86[a]	75.50 ± 2.57[b]	19.72 ± 11.42[c]	0.03
GPT mg pyruvate per min per g	11.52 ± 2.27[a]	7.45 ± 1.60[ab]	3.33 ± 0.037[b]	0.001

[a] Letters indicate degree of significant based on Tukey's HSD tests between different treatments and control. Letter (a) mean high significant, and letter (c) mean low significant, while the same letters are not significantly different.

3.5. Impact of the nanocomposites on the larval protein and enzymes

The 4th larval instars exposed to the nanocomposites were used to investigate the biomarker enzymes after detection of their protein from the normal and treated larvae. A significant difference was observed between the protein contents of the control and exposed larvae ($p \leq 0.016$). The protein value of the treated larvae was decreased to 19.29 and 5.87 mg g^{-1} in case of MnCoO and MnCoO/CNTs, respectively, compared to 32.87 mg g^{-1} for control larval (Table 2). This work showed direct toxicity on the protein synthetic machinery, where MnCoO/CNTs achieved a higher effect than that of MnCoO. Moreover, protein has a main role in the insects during metamorphosis involving epidermal formation and synthesis of chitin, but when insects are exposed to the insecticide, protein level changes in the

Fig. 11 SEM images of the control fourth larval instar of mosquito *Cx. pipiens*: (a) whole body with normal morphological features; (b) head capsule and mouth parts; (c) abdominal segments; (d) respiratory opening (siphon and gills) (Abd: abdomen; H: head; Ha: head hair; G: gill; Mb: mouth brushes; Pt: pectin teeth; S: siphon).
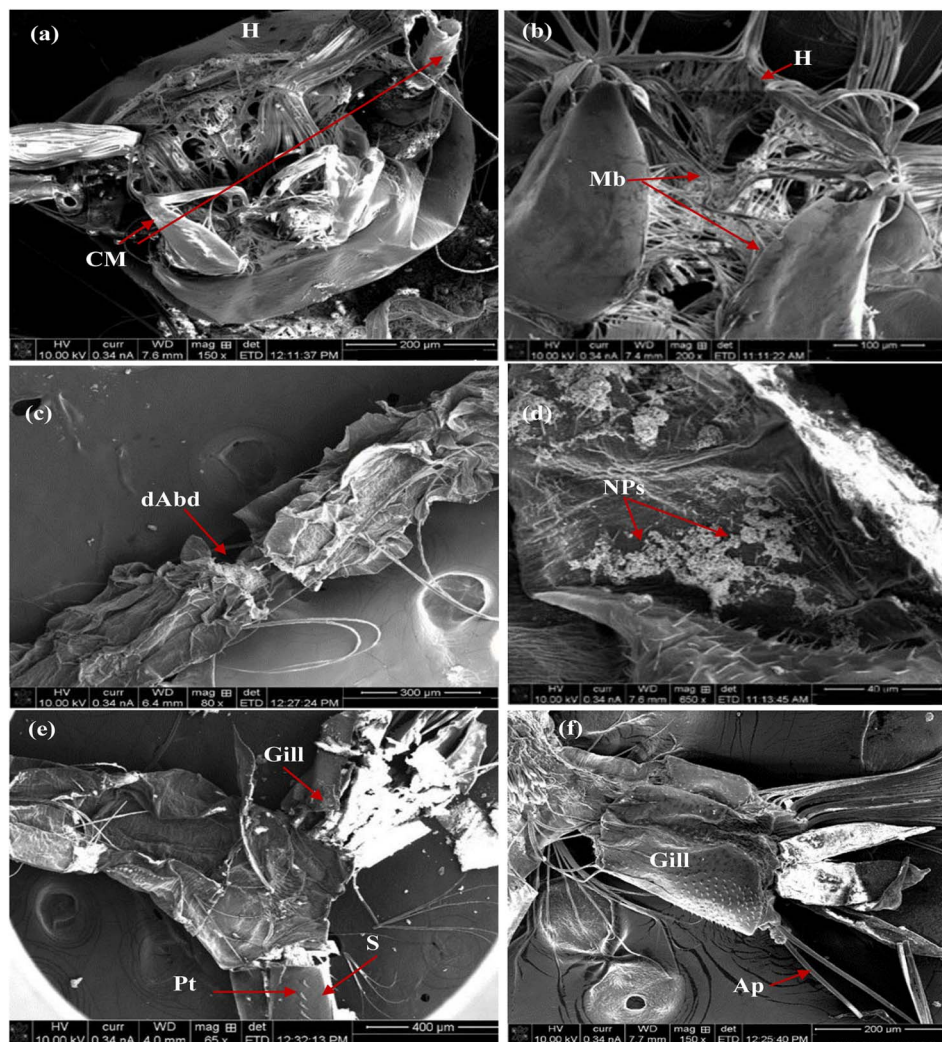
Fig. 12 SEM images of fourth larval instar of mosquito *Cx. pipiens* treated with MnCoO NPs at an amount of 50 ppm, for 24 h incubation period: (a and b) malformed mouth brushes and chewing mouthparts; (c and d) damaged abdominal segments; (e and f) respiratory gills and siphon were destroyed. (Ap: anal papilla; dAbd: damaged abdominal segments; CM: chewing mouthparts; H: head; G: gill; Mb: mouth brushes; NPs: nanoparticles; Pt: pectin teeth; S: siphon).

whole body can be triggered by down-regulation or up-regulation.[49,50] As summarized in Table 2, the level of acid phosphatase activity drastically decreased from 1041.61 of control larvae to 504.72 and 555.36 U g^{-1} upon exposure to MnCoO and MnCoO/CNTs, respectively. Additionally, the value of alkaline phosphatase declined from 2113.37 for control to 74.86 and 200.25 U g^{-1} in the 4th larval instar of *C. pipiens* treated with MnCoO and MnCoO/CNTs, respectively for an equal length of time. Many physiological processes like metabolism and cell signaling are related to the activity of these enzymes.[50]

In a previous study, Koodalingam *et al.*[51] have shown the effect of kernel extract of *Sapindus emarginatus* on acid and alkaline phosphatases of immature stages of the mosquito *Aedes aegypti*. Herein, the activity of acetylcholinesterase in larvae exposed to the nanomaterials was inhibited to release a small amount of enzyme; for the control larvae, this was 1858.92 U g^{-1}, whereas for the treated larvae, this was 815.57 and 264.49 U g^{-1} for MnCoO and MnCoO/CNTs, respectively.

The inhibition of esterase activity may be associated with the binding of nanocomposites to the acetylcholinesterase receptor binding site, preventing the release of acetylcholinesterase enzymes to break down acetylcholine substrates and it leads to the accumulation of acetylcholine at the postsynaptic junction, resulting in the opening of the sodium channel as well as helping the continuous passing of sodium ions to make a permanent stimulation state in the tested mosquito. Therefore, the lack of coordination at the point of the neuromuscular system causes larval death.[52,53] The exposure of mosquito larvae to MnCoO and MnCoO/CNTs results in the reduction of α-carboxylesterase and β-carboxylesterase activities compared to the control. The findings indicate that the nanomaterials obstruct the involvement of esterase, which is necessary for the detoxification of xenobiotics and development of insect's resistance against insecticides.[54,55] The GOT activity decreased to 75.50 ± 2.57 mg pyruvate per min per g with MnCoO and extremely declined to 19.72 ± 11.42 mg pyruvate per min per g with
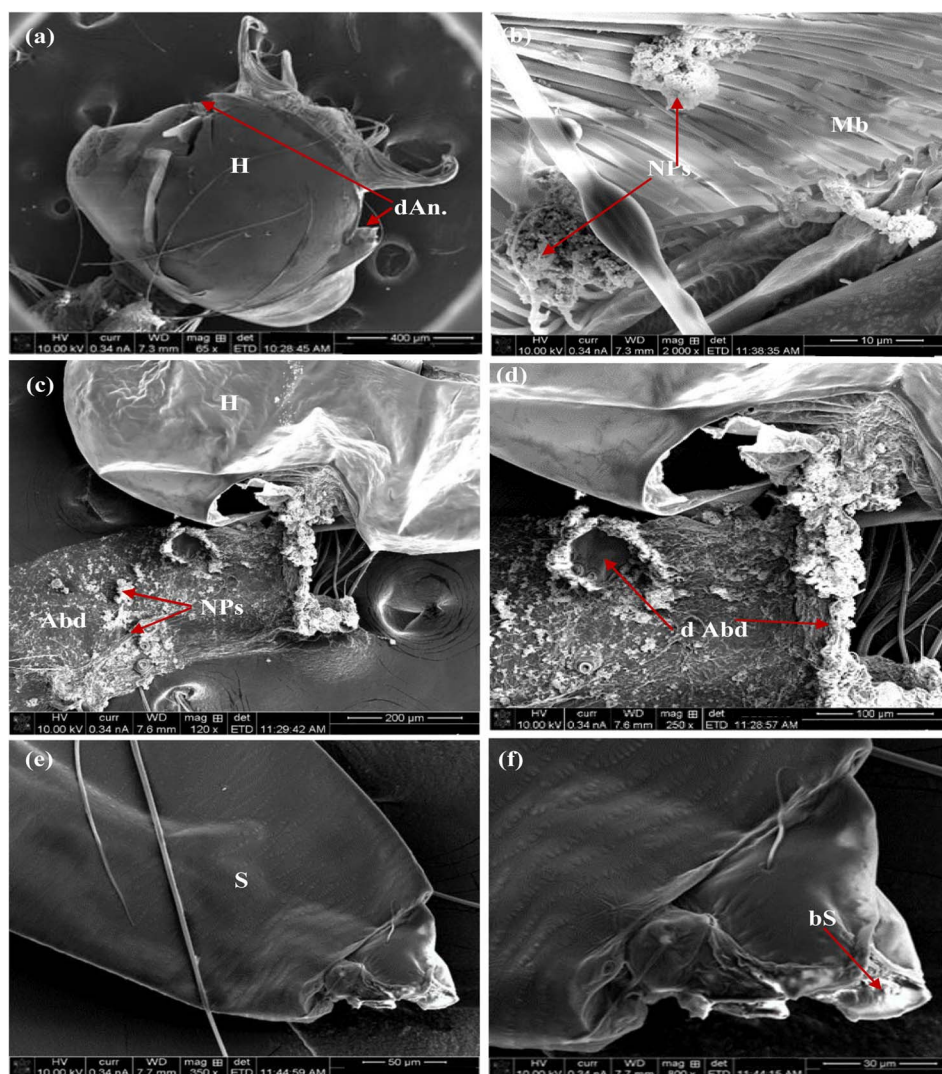
MnCoO/CNTs compared to 169.47 ± 1.86 mg pyruvate per min per g for the control. Moreover, GPT enzyme activity was inhibited by MnCoO and MnCoO/CNTs to 7.45 ± 1.60 and 3.33 ± 0.037 mg pyruvate per min per g, respectively. This result is in agreement with the reduction of GOT and GPT in 4th larval instars of *Tribolium granarium* after treatment with plant oils. The GPT activity was also inhibited in palm weevil *Rhynchophorus ferrugineus* by certain insecticidal compounds.[53,55] The current study confirms that the nanoparticles cause damage to intracellular organelles or disturb their ordinary physiological functions, leading to alteration in the entire organ system, sequentially, leading to larval death.

3.6. Morphological study of the infected larvae

The larvicidal activity was examined by applying a small amount of the nanoparticles on the 4th larval instar of *C. pipiens* larvae.

Fig. 11 describes the SEM images of untreated larvae. As demonstrated, whole body with normal morphological features (Fig. 11a), the normal larval head capsule and mouthparts is shown in Fig. 11b, and abdominal segments, respiratory gill and siphon without any deterioration in Fig. 11c and d.

Furthermore, Fig. 12 illustrates the impact of MnCoO on the larval body parts. This effect was observed as the malformation of chewing mouthparts and mouth brushes in the head region (Fig. 12a and b), destruction of the abdominal region, accumulation of nanoparticles on their cuticle (Fig. 12c and d), and damaging of respiratory gills and siphon (Fig. 12e and f). Moreover, the influence of the nanocomposite MnCoO/CNTs is shown in Fig. 13. Deformations in different body parts including broken head with NPs accumulated in mouth brushes (Fig. 13a and b), high density of nanomaterials on the abdominal cuticle and rupture of abdominal segment (Fig. 13c and d), and blocking of respiratory siphon with NPs,

Fig. 13 SEM images of fourth larval instar of mosquito *Cx. pipiens* treated with MnCoO/CNTs: (a and b) broken head with NPs accumulated in mouth brushes; (c and d) abdominal segments damaged with NPs; (e and f) respiratory siphon was blocked. (Ap: anal papilla; dAbd: damage abdominal segments; b S: block siphon; d An: damaged antennae; CM: chewing mouthparts; H: head; Mb: mouth brushes; NPs: nanoparticles; S: siphon).

which leads to larval suffocation (Fig. 13e and f), were observed.[54–56]

4 Conclusions

MnCoO and MnCoO/CNT nanocomposites have been successfully prepared via a chemical co-precipitation route. Structural, molecular interaction, and purity of the nanomaterials were identified using XRD patterns, Raman spectra, and EDX spectra. The samples exhibited a weak crystalline degree, in which a binary phase of MnO_2 and Co_3O_4 was observed in the XRD spectrum. SEM and TEM micrographs were obtained to visualize the microstructure of the nanoparticles, indicating that MnCoO/CNT nanoflakes have a large surface area. The energy gap (E_g) of the thin films was evaluated from the UV-vis spectrum to be 3.98 eV, which decreased to 3.92 eV with CNT dopants. The study of photocatalysis revealed that MnCoO/CNTs show higher photodegradation activity for methyl orange (MO) dye than that of the pure MnCoO catalyst. Under the UV impact, the composite catalyst achieved an efficiency 90.97% over 0.6 g L^{-1} within 50 min depending on the CNT support. In the biological section, the nanocomposites disturbed the activities of enzymes acid and alkaline phosphatase, acetylcholinesterase, β & α-carboxylesterases, GOT, and GPT, which have different physiological functions in the insect body. Disorder of the enzymatic activities can be understood as a non-lethal influence of the tested compounds but eventually lead to larval death. In conclusion, the most potent nanocomposite for inhibiting enzyme activities was MnCoO/CNT causing malformation of the morphological structure, resulting in larval death, in addition to its high efficiency for the photocatalytic degradation of methyl orange dye.

Author contributions

All authors contributed to the planning and implementation of the research, to the analysis and presentation of the results and to the writing and editing of the manuscript equally. R. A. Mohamed is responsible for funding acquisition and the corresponding author.

Conflicts of interest

The authors declare that they have no competing interests.

Acknowledgements

References

1 D. Mondal, S. Das, B. K. Paul, D. Bhattacharya, D. Ghoshal, A. L. Gayen, K. Das, S. Das, et al., Size engineered Cu-doped α-MnO_2 nanoparticles for exaggerated photocatalytic activity and energy storage application, Mater. Res. Bull., 2019, **115**, 159–169.

2 H. M. Hamama, O. H. Zyaan, O. A. A. Ali, D. I. Saleh, H. A. El-Akkad, M. T. El-Saadony and S. M. Farag, Virulence of entomopathogenic fungi against Culex pipiens: impact on biomolecules availability and life table parameters, Saudi J. Biol. Sci., 2022, **29**(1), 385–393.

3 E. Beheshti, H. Doryani, M. R. Malayeri, M. Riazi, et al., Asphaltene stability during heptane injection in a glass micromodel in the presence of Co_3O_4 nanoparticles, J. Pet. Sci. Eng., 2021, **205**, 108839.

4 M. Siddique, N. Fayaz, M. Saeed, et al., Synthesis, characterization, photocatalytic activity and gas sensing properties of zinc doped manganese oxide nanoparticles, Phys. B, 2021, **602**, 412504.

5 X. Liang, F. Wang, M. Chen, X. Xia, et al., Carbon nanotubes branch on cobalt oxide nanowires core as enhanced high rate cathodes of alkaline batteries, Ceram. Int., 2018, **44**, 16791–16798.

6 S. A. El-Khodary, I. S. Yahia, H. Y. Zahran, M. Ibrahim, et al., Preparation of polypyrrole-decorated MnO_2/reduced graphene oxide in the presence of multi-walled carbon nanotubes composite for high performance asymmetric supercapacitors, Phys. B, 2019, **556**, 66–67.

7 I. R. Abdel-Shafi, E. Y. Shoeib, S. S. Attia, J. M. Rubio, Y. Edmardash, A. A. El-Badry, et al., Mosquito identification and molecular xenomonitoring of Lymphatic Filariasis in selected endemic areas in Giza and Qualioubiya governorates. Egypt, J. Egypt. Soc. Parasitol., 2016, **46**, 87–94.

8 A. S. Darwish, M. A. Sayed, A. Shebl, et al., Cuttlefish bone stabilized Ag_3VO_4 nanocomposite and its Y_2O_3-decorated form: waste-to value development of efficiently ecofriendly visible-light photoactive and biocidal agents for dyeing, bacterial and larvae depollution of Egypt's wastewater, J. Photochem. Photobiol., A, 2020, **401**, 112749.

9 K. S. Hamadah, Disturbance of phosphatase and transaminase activities in grubs of the red palm weevil Rhynchophorus ferrugineus (Coleoptera: Curculionidae) by certain insecticidal compounds, J. Basic Appl. Zool., 2019, **80**, 52.

10 C. E. Wheelock, G. Shan, J. Ottea, et al., Overview of carboxylesterase and their role in the metabolism of insecticides, J. Pestic. Sci., 2005, **30**, 75–83.

11 K. Sonu, S. H. Puttaiah, V. S. Raghavan and S. S. Gorthi, Photocatalytic degradation of MB by TiO2: studies on recycle and reuse of photocatalyst and treated water for seed germination, Environ. Sci. Pollut. Res., 2021, **28**, 48742–48753.

12 J. G. Gornall, G. J. Bardwill, M. M. David, et al., Determination of serum protein by mean of Biuret reaction, J. Biol. Chem., 1949, **117**, 751–766.

13 D. R. Simpson, D. L. Bulland, D. A. Linquist, et al., A semi micro technique for estimation of cholinesterase activity in boll weevils, Ann. Entomol. Soc. Am., 1964, **57**, 367–371.

14 M. E. A. Powell and M. J. H. Smith, The determination of serum acid and alkaline phosphatase activity with 4-aminoantipyrine (AAP), *J. Clin. Pathol.*, 1954, **7**(3), 245.

15 K. Van Asperen, A study of housefly esterase by means of sensitive colorimetric method, *J. Insect Physiol.*, 1962, **8**, 401–416.

16 S. M. Reitman and S. Frankel, A colorimetric method for determination of serum glutamic pyruvic transaminase, *Am. J. Clin. Pathol.*, 1957, (28), 56–63.

17 X. Wu, F. Yang, H. Dong, J. Sui, Q. Zhang, J. Yu, Q. Zhang, L. Dong, *et al.*, Controllable synthesis of MnO_2 with different structures for supercapacitor electrodes, *J. Electroanal. Chem.*, 2019, **848**, 113332.

18 S. Farhadi, J. Safabakhsh, P. Zaringhadam, *et al.*, Synthesis, characterization, and investigation of optical and magnetic properties of cobalt oxide (Co_3O_4) nanoparticles, *J. Nanostruct. Chem.*, 2013, **3**, 69.

19 Y. Liang, Y. Yang, K. Xu, T. Yu, Q. Peng, S. Yao, C. Yuan, *et al.*, Controllable preparation of faceted Co_3O_4 nanocrystals@MnO_2 nanowires shish-kebab structures with enhanced triethylamine sensing performance, *Sens. Actuators, B*, 2020, **304**, 127358.

20 B. Saravanakumar, X. Wang, W. Zhang, L. Xing, W. Li, *et al.*, Holey two dimensional manganese cobalt oxide nanosheets as a high performance electrode for super capattery, *Chem. Eng. J.*, 2019, **373**, 547–555.

21 T. Wang, D. Song, H. Zhao, J. Chen, C. Zhao, L. Chen, W. Chen, J. Zhou, E. Xie, *et al.* Facilitated transport channels in carbon nanotube/carbon nanofiber hierarchical composites decorated with manganese dioxide for flexible supercapacitors, *J. Power Sources*, 2015, **274**, 709–717.

22 M. Manickam, V. Ponnuswamy, C. Sankar, R. Suresh, *et al.*, Cobalt oxide thin films prepared by NSP technique: impact of molar concentration on the structural, optical, morphological, and electrical properties, *Optik*, 2016, **127**, 5278–5284.

23 G. Cabello and R. A. Davoglio, Inorganic frameworks based on bimetallic encapsulated in hollow MnO_2 structures, *Appl. Catal., B*, 2017, **218**, 192–198.

24 S. A. Makhlouf, Z. H. Bakr, K. I. Aly, M. S. Moustafa, *et al.*, Structural, electrical, and optical properties of Co_3O_4 nanoparticles, *Superlattices Microstruct.*, 2013, **64**, 107–117.

25 A. M. Abdel-Raoof, A. O. Osman, E. A. El-Desouky, A. Abdel-Fattah, R. F. Abdul-Kareema, E. Elgazzar, *et al.*, Fabrication of an (α-Mn_2O_3: Co)-decorated CNT highly sensitive screen printed electrode for the optimization and electrochemical determination of cyclobenzaprine hydrochloride using response surface methodology, *RSC Adv.*, 2020, **10**, 24985.

26 P. Rajkumar and B. K. Sarma, Substrate dependent structural variations of biomimetic carbonated hydroxyapatite deposited on glass, Ti and sputtered ZnO thin films, *Mater. Charact.*, 2022, **191**, 112120.

27 H. Huang, Q. Xue, Y. Zhang and Y. Chen, Two-dimensional cobalt prussian blue nanosheets: template-directed synthesis and electrocatalytic oxygen evolution property, *Electrochim. Acta*, 2020, **333**, 135544.

28 C. Cui, G. Du, K. Zhang, T. An, B. Li, X. Liu, Z. Liu, *et al.*, Co_3O_4 nanoparticles anchored in MnO_2 nanorods as efficient oxygen reduction reaction catalyst for metal-air batteries, *J. Alloys Compd.*, 2020, **814**, 152239.

29 M. M. Makhlouf, Preparation and optical characterization of MnO_2 nano thin films for application in heterojunction photodiodes, *Sens. Actuators, A*, 2018, **279**, 145–156.

30 E. Elgazzar, Improvement the efficacy of Al/CuPc/n-Si/Al Schottky diode based on strong light absorption and high photocarriers response, *Mater. Res. Express*, 2020, **7**, 095102.

31 N. M. Hosny and A. Dahshan, Facile synthesis and optical band gap calculation of Mn_3O_4 nanoparticles, *Mater. Chem. Phys.*, 2012, **137**, 637–643.

32 R. Venkatesha, C. R. Dhas, R. Sivakumarb, T. Dhandayuthapanib, P. Sudhagar, C. Sanjeeviraja, A. M. Raj, *et al.*, Analysis of optical dispersion parameters and electrochromic properties of manganese-doped Co_3O_4 dendrite structured thin films, *J. Phys. Chem. Solids*, 2018, **122**, 118–129.

33 B. K. Pandey, A. K. Shahi, R. Gopal, *et al.*, Synthesis, optical properties and growth mechanism of MnO nano structures, *Appl. Surf. Sci.*, 2013, **283**, 430–437.

34 N. C. Martins, J. Ângelo, A. V. Girão, T. Trindade, L. Andrade, A. Mendes, *et al.*, N-doped carbon quantum dots/TiO_2 composite with improved photocatalytic activity, *Appl. Catal., B*, 2016, **193**, 67–74.

35 S. Zhu, J. Zhang, C. Qiao, S. Tang, Y. Li, W. Yuan, B. Li, L. Tian, F. Liu, R. Hu, H. Gao, H. Wei, H. Zhang, H. Sun, B. Yang, *et al.*, Strongly green-photoluminescent graphene quantum dots for bioimaging applications, *Chem. Commun.*, 2011, **47**, 6858.

36 C. Yang, P. Wang, J. Li, Q. Wang, P. Xu, S. You, Q. Zheng and G. Zhang, Photocatalytic PVDF ultrafiltration membrane blended with visible-light responsive Fe(III)-TiO_2 catalyst: degradation kinetics, catalytic performance and reusability, *Chem. Eng. J.*, 2021, **417**, 129340.

37 A. K. Dutta, U. K. Ghorai, K. K. Chattopadhyay and D. Banerjee, Removal of textile dyes by carbon nanotubes: a comparison between adsorption and UV assisted photocatalysis, *Phys. E*, 2018, **99**, 6–15.

38 Y. Li, Y. Hu, Y. Zhao, G. Shi, L. Deng, Y. Hou, L. Qu, *et al.*, An electrochemical avenue to green-luminescent graphene quantum dots as potential electron-acceptors for photovoltaics, *Adv. Mater.*, 2011, **23**, 776.

39 D. Chaudhary, S. Singh, V. Vankar, N. Khare, *et al.*, ZnO nanoparticles decorated multi-walled carbon nanotubes for enhanced photocatalytic and photoelectrochemical water splitting, *J. Photochem. Photobiol., A*, 2018, **351**, 154–161.

40 D. Chaudhary, S. Singh, D. V. Vankar, N. Khare, *et al.*, ZnO nanoparticles decorated multi-walled carbon nanotubes for enhanced photocatalytic and photoelectrochemical water splitting, *J. Photochem. Photobiol., A*, 2018, **351**, 154–161.

41 K. Wetchakuna, N. Wetchakunb and S. Sakulsermsuk, An overview of solar/visible light-driven heterogeneous photocatalysis for water purification: TiO_2- and ZnO-based

photocatalysts used in suspension photoreactors, *J. Ind. Eng. Chem.*, 2019, **71**, 19–49.

42 M. R. Al-Mamun, K. T. Hossain, S. Mondal, M. A. Khatun, M. S. Islam and M. Z. Khan, Synthesis, characterization, and photocatalytic performance of methyl orange in aqueous TiO_2 suspension under UV and solar light irradiation, *S. Afr. J. Chem. Eng.*, 2022, **40**, 113–125.

43 X. Yan, X. Cui, B. Li, L. Li, *et al.*, Large, solution-processable graphene quantum dots as light absorbers for photovoltaics, *Nano Lett.*, 2010, **10**, 1869.

44 C. M. Luk, L. B. Tang, W. F. Zhang, S. F. Yu, K. S. Teng, S. P. Lau, *et al.*, An efficient and stable fluorescent graphene quantum dot–agar composite as a converting material in white light emitting diodes, *J. Mater. Chem.*, 2012, **22**, 22378.

45 X. Qu, M. Liu, J. Yang, C. Wang, H. Meng, S. Li, L. Shi, F. Du, *et al.*, A novel ternary TiO_2/CQDs/BiOX (X = Cl, Br, I) heterostructure as photocatalyst for water purification under solar irradiation, *J. Solid State Chem.*, 2018, **264**, 77–85.

46 Z. Zarnegar, J. Safari, Z. Mansouri-Kafroudi, *et al.*, Environmentally benign synthesis of polyhydroquinolines by Co_3O_4–CNT as an efficient heterogeneous catalyst, *Catal. Commun.*, 2015, **59**, 216–221.

47 A. Kanwal, S. Sajjad, S. A. K. Leghari and M. N. Khan, Strong interfacial charge transfer between hausmannite manganese oxide and alumina for efficient photocatalysis, *Chin. J. Chem. Eng.*, 2021, **33**, 147–159.

48 S. A. Kadam, S. A. Thomas, Y. R. Ma, L. M. Jose, D. Sajan and A. Aravind, Investigation of adsorption and photocatalytic behavior of manganese doped zinc oxide nanostructures, *Inorg. Chem. Commun.*, 2021, **134**, 108981.

49 E. Parthib, M. Ramachandra, M. Jayakumar, R. Ramanibai, *et al.*, Biocompatible green synthesized silver nanoparticles impact on insecticides resistant developing enzymes of dengue transmitted mosquito vector, *SN Appl. Sci.*, 2019, **1**, 1282.

50 M. Torres and H. J. Forman, Signal transduction, 2006, *Encycl. Respir. Med.*, pp. 10–18.

51 A. Koodalingam, P. Mullainadhan, M. Arumugam, *et al.*, Effects of extract of soapnut Sapindus emarginatus on esterases and phosphatases of the vector mosquito *Aedes aegypti* (Diptera: Culicidae), *Acta Trop.*, 2011, **118**, 27–36.

52 D. Aygun, Z. Doganay, L. Altintop, H. Guven, M. Onar, T. Deniz, T. Sunter, *et al.*, Serum acetylcholinesterase and prognosis of acute organophosphate poisoning, *J. Toxicol.*, 2002, **40**, 903–910.

53 S. H. P. P. Karunaratne and J. Hemingway, Different insecticides select multiple carboxylesterase isoenzymes and different resistance levels from a single population of *Culex quinquefasciatus*, *Pestic. Biochem. Physiol.*, 1996, **54**, 4–11.

54 M. W. F. Younes, S. E. Othman, M. A. Elkersh, N. S. Youssef, A. Gihan, G. A. Omar, *et al.*, Effect of seven plant oils on some biochemical parameters in kh beetle *Trogoderma granariumeverts* (Coleoptera: Dermestidae), *Egypt. J. Exp. Biol. (Zoo.)*, 2011, **7**(1), 53–61.

55 G. Benelli, A. Caselli, A. Canale, *et al.*, Nanoparticles for mosquito control: Challenges and constraints, *J. King Saud Univ. Sci.*, 2016, **29**, 424–435.

56 G. Benelli, Mode of action of nanoparticles against insects, *Environ. Sci. Pollut. Res.*, 2018, **25**, 12329–12341.